Effect of the liquid-vacuum transition on the relative abundances of amino and fatty acids sought as biosignatures on icy ocean worlds

Marc Neveu[1,2,*], Alexandria Aspin[3,*], Mariam Naseem[1], and Ziming Yang[3]

[1] University of Maryland, College Park, MD, USA
[2] NASA Goddard Space Flight Center, Greenbelt, MD, USA
[3] Department of Chemistry, Oakland University, Rochester, MI, USA
[*] These authors contributed equally to this manuscript.

Corresponding authors:

Marc Neveu (marc.f.neveu@nasa.gov)
Ziming Yang (zimingyang@oakland.edu)

Abstract

Interpreting measurements by robotic missions searching for signs of life in material erupted by cryovolcanic ocean worlds (e.g., Enceladus, Europa, Ceres) requires linking the composition of this material to that of its subsurface liquid source. Irrespective of the properties of –and processes along– the path of ejection, material erupted on airless worlds undergoes a transition from liquid to vacuum. Here, we investigate experimentally the effect of a direct transition from liquid to vacuum environments on the relative abundances of amino and carboxylic (fatty) acids, a metric used to distinguish between biological and abiotic sources for these compounds. Amino acids were dissolved in parent solutions prepared with 1 wt.% NaCl and pH 9–10 to match properties inferred from Enceladus plume grains. Compositional analysis of the dry solids resulting from the injection of this solution into vacuum indicates a < 50% change in amino acid abundances relative to glycine. Injection of two fatty acids, phenylacetic acid (soluble and undersaturated in the parent solution) and palmitic acid (insoluble and supersaturated) resulted in a change of less than a factor of 7 in their relative abundances. At this bulk scale (all grains aggregated together), proportions of amino and fatty acids were sufficiently conserved to allow distinction between end-member example biological and abiotic sources. We did not find strong correlations between the relative enrichment or depletion of amino or fatty acids with molecular properties such as molecular mass, hydrophobicity, functionality, or charge, other than high under- or supersaturation. Most of the organic residue was deposited along the experimental injection path, which suggests that cryovolcanic conduit walls on icy ocean worlds may be enriched in organic material relative to material having undergone the liquid-vacuum transition.

Keywords

Amino acids, fatty acids, ocean worlds, biosignatures, Enceladus, Ceres

1. Introduction

In our Solar System, several icy moons and dwarf planets harbor subsurface oceans (Hendrix et al., 2019). A few of these ocean worlds display surface or plume activity indicating that subsurface liquid material is being expressed at or above the surface. These include Enceladus (Porco et al., 2006; Villanueva et al., 2023a), Ceres (Ruesch et al., 2016), and, perhaps, Europa (e.g., Roth et al., 2014; Quick et al., 2017; Villanueva et al., 2023b, and references therein). The detection or expectation of sources of bioavailable energy and bioessential elements from the interiors of Enceladus and Europa, respectively (Hand et al., 2009; Hsu et al., 2015; Waite et al., 2017; Postberg et al., 2018a; Khawaja et al., 2019; Postberg et al., 2023; Vance et al., 2023; Villanueva et al., 2023b), makes them prime places to search for life without having to access the (sub)surface (Cable et al., 2020, 2021; Hand et al., 2022; MacKenzie et al., 2022).

Any search for signs of life and contextual information in erupted materials requires inferring, from the measurements, characteristics of their subsurface liquid source and mechanisms for release to the surface and subsequent processing (e.g., radiation exposure at the surface or in orbit) before collection. The nonvolatile solute composition may be preserved through eruption, e.g., if the liquid source composition is frozen in due to rapid cooling (Thomas et al., 2019; Vu et al., 2020, 2023), albeit (1) with bulk concentration or dilution due to loss of water to vaporization or condensation of water sublimated from a solid source (Postberg et al., 2018b; Khawaja et al., 2019), and (2) at spatial scales larger than individual ice grains (Fox-Powell & Cousins, 2021).

Erupted material could also undergo broader compositional changes. In the plume of Enceladus, water vapor (90–99 mass% of the plume at ~100 km altitude; Postberg et al., 2018b) dominates over ice. Plume ice grains falling back to the surface may not, alone, explain this high

vapor enrichment compared to the ≈1:7.5 vapor:ice proportions expected from exposing liquid water at the triple point to vacuum (Spencer et al., 2018). This suggests a role for additional processes, such as accretion of grains on conduit walls or ice sublimation from these walls, which might distill or cycle nonvolatile material between the subsurface liquid and the surface vent. Along the way, moderately volatile organic compounds might be selectively adsorbed onto ice (Bouquet et al., 2019; Khawaja et al., 2019). The plume also contains percent-level gases other than water: e.g., CO_2, CH_4, N_2 or CO, H_2, NH_3, and HCN (Waite et al., 2017; Peter et al., 2023). These volatile compounds are likely exsolved from the fluid, which can alter such fundamental chemical properties of erupted material as its pH (e.g., via CO_2-carbonate equilibria), affecting the molecular form of most chemical elements in water (Fifer et al., 2022). These processes may alter material properties that search-for-life missions seek to measure.

The overall process certain to occur during eruption on airless ocean worlds is the phase transition of water from the liquid phase to vapor and ice in vacuum (hereafter "liquid-vacuum transition"). At Enceladus, this transition occurs in subsurface plume source conduits (Schmidt et al., 2008; Nakajima and Ingersoll, 2016; Ingersoll & Nakajima, 2016). At Ceres, it may occur as erupted material flows onto the surface (Ruesch et al., 2016, 2019; Scully et al., 2020). At Europa, both eruption styles are possible (e.g., Fagents, 2003; Roth et al., 2014).

Here we investigate whether, and to what extent, the liquid-vacuum transition can change relative abundances of amino and carboxylic (fatty) acids in erupted material targeted by search-for-life measurements (Dorn et al., 2003; MacKenzie et al., 2022; Hand et al., 2022). Amino and

fatty acids that differ in their volatility, solubility, charge, or other physicochemical properties may be partitioned differently in material transported into vacuum than in its aqueous source.

We report the results of experimental injections of aqueous solutions of amino and fatty acids into a vacuum chamber, using a procedure described in Section 2. Despite significant deposition along the fluid path, we find moderate changes in relative proportions (< 50% relative to glycine) of amino acids, and less constrained but slightly larger changes in those of fatty acids, when considering material aggregated by section of the fluid path (Section 3). We discuss possible causes for these changes in Section 4. We find them small compared to differences in relative abundance patterns between example biological and abiotic sources. We conclude in Section 5 on the prospects for recognizing evidence of life based on relative abundances of amino and fatty acids in materials having undergone the liquid-vacuum transition.

2. Materials and Methods

2.1. Injection of liquid into vacuum

To inject aqueous solutions into vacuum, we designed and built an experimental setup at NASA's Goddard Space Flight Center (Fig. 1). This setup consists of an organic-clean (no elastomer seals), bakeable vacuum chamber (Sharon Vacuum Co., Inc.) into which a solution is injected using a low-flow valve. The resulting abundant water vapor is evacuated by a turbo mechanical pump (Agilent TwisTorr 74 FS) backed by a dry scroll forepump (Agilent IDP-7), and also partly condensed on a copper plate cooled by a Stirling cryocooler (Sunpower/Ametek Cryotel MT). The condensed fraction of the vapor can be recovered post-injection for analysis. The rest of the chamber is at room temperature, as is, roughly, the injection line (see below). An aluminum collection cup of diameter ≈ 5 cm, of the type typically used as a weighing container, was placed

inside the chamber, facing the port through which material was injected, on a stand of ultra-high vacuum aluminum foil (All Foils, Inc.) that also shielded the gauges and pumps from particles. A second cup was placed at the chamber bottom to collect material that had fallen from the port-facing cup.

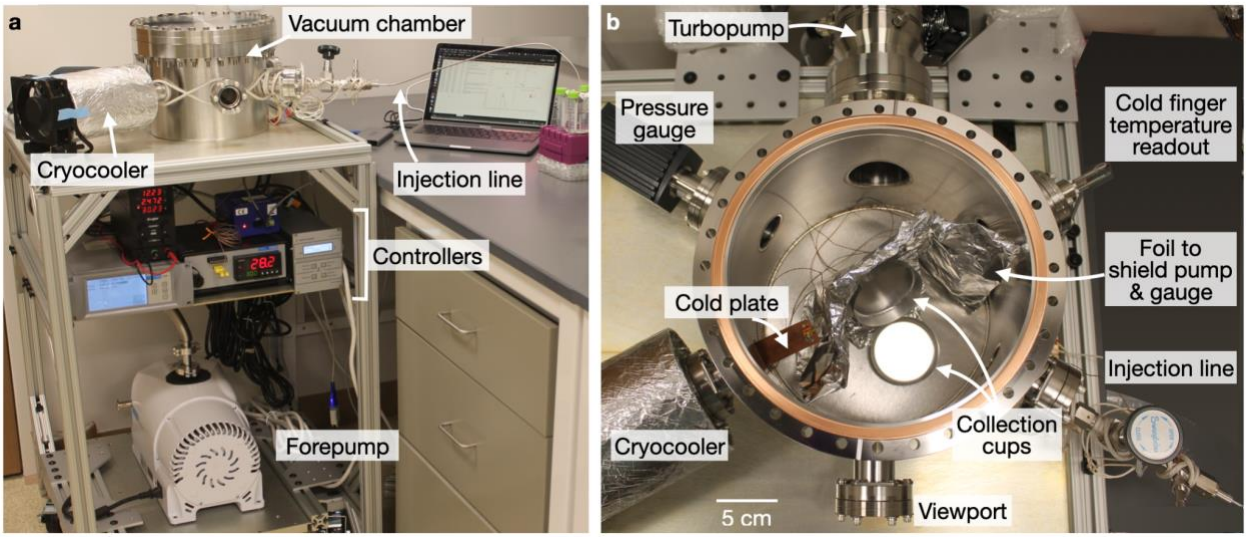

Figure 1. (a) *Overview of the experimental setup with the injected solution to the right, on the purple stand.* ***(b)*** *Top view of the chamber with, inside, a cryocooled copper plate (to condense part of the water vapor), aluminum collection cups, and aluminum foil stand/shield.*

The chamber's base pressure is 5×10^{-7} Torr. Upon injection of liquid, it increases along the water vapor pressure curve at the cryocooled plate temperature. The pressure along this curve was controlled by adjusting the fluid flow rate using the low-flow valve to remain below the triple point pressure of H_2O (P_t = 611 Pascals = 4.6 Torr), ensuring the injected material underwent a complete liquid-vacuum transition. When depressurization brings the injected water to P_t, water partially boils; the corresponding enthalpy of phase change ($L_{vap} \approx 2500$ kJ kg^{-1}) would tend at thermodynamic equilibrium to freeze $L_{vap} / L_{freeze} \approx 7.5$ times as much water, since the enthalpy of

138 freezing is L_{freeze} = 334 kJ kg^{-1} (Spencer et al., 2018). Freezing in the injection line could cause ice
139 to clog it, resulting in an ice-vacuum sublimation interface rather than the liquid-vacuum transition
140 we sought to investigate. Although dissolved salts and supercooling could delay ice formation
141 (e.g., Pruppacher & Klett, 2010), in pilot injections we noticed segments of the injection line
142 becoming cold, and therefore opted to heat the injection line to 30±15ºC to prevent freezing up to,
143 and excluding, the chamber flange (see Fig. 2).
144
145 Injection rates ranged from 1 to 25 mL h^{-1}. Lower flow rates resulted in impractically long
146 injection times (weeks for a ≥ 200 mL solution). Higher flow rates resulted in vapor loads above
147 P_t. The ratio of flow rate to conduit cross-sectional area up to the flange, (1–25 g h^{-1}) / (7.9–32
148 mm^2), is 0.009–0.88 kg m^{-2} s^{-1}. It is similar to the ratio obtained for one of ≈100 vents (Porco et
149 al., 2014), meters in scale (Goguen et al., 2013; Ingersoll & Nakajima, 2016), that together provide
150 a flow rate of 300 kg s^{-1} relevant to Enceladus (Villanueva et al., 2023a): (300 kg s^{-1}) / 100 / (3–
151 300 m^2) = 0.01–1 kg m^{-2} s^{-1}. The length:diameter ratio of section of the injection line depressurized
152 below P_t, about (15 cm)/(3 mm) = 50, is at the low end of the ratio estimated for Enceladus
153 conduits, ~(0.5–1 km)/(1–10 m) = 50–1000, since the neutral buoyancy level of liquid water in
154 pure water ice would be at ≈10% of the depth of a ≈5–10 km-thick ice shell in the south polar
155 region (Hemingway & Mittal, 2019).
156
157 Other aspects of this experimental setup differ from known or expected properties of
158 eruption conduits through Enceladus' ice shell in such a way that grain-wall interactions are not
159 accurately emulated. First, experimental conduit walls are not made of ice, but stainless steel.
160 Second, the experimental ratio of grain velocity to conduit length, i.e., residence time in the

conduit, is three to four orders of magnitudes lower in the experimental setup (see Section S1 and below).

The injected liquid is expected to have turned to vapor and droplets of size d ranging from μm to mm resulting from burst bubbles (e.g., Cochran et al., 2016; Porco et al. 2017, and references therein) that partially vaporized. The energy loss from vaporization can freeze a droplet core of diameter d in $t_{freeze} \sim 0.03$ (d / 1 mm) second (Steddum, 1971; Miller et al., 2022), i.e., ~10 to 10^5 μs. Dissolved salt may delay complete freezing, but the low salt concentration in our solutions (~1 wt.%, see below) and the low energy loss needed to cool from 273 K to the water-salt eutectic temperature ($C_p \Delta T \approx 80$ kJ kg^{-1}, i.e., ~25% of L_{freeze}, where C_p is the heat capacity of water and ΔT the temperature contrast, about 20 K for NaCl) suggest this delay is not significant. Supercooling to as low as 230 K (Pruppacher & Klett, 2010) may cause another ~25% delay.

The fluid cooling rate can be roughly estimated as the difference between the room or conduit temperature and the H_2O triple point temperature ($T_{triple} = 273$ K), about 25 K, divided by an inferred residence time of ~0.005 s (Section S1), i.e., ~10^3 K s^{-1}. Such cooling rates have been invoked for ocean droplets undergoing ejection on Enceladus (Section 4.4 of Fox-Powell & Cousins, 2021, and references therein). However, they are much higher than a bulk fluid cooling rate of $(T_{triple}–T_{vent})/t \sim 0.1$ K s^{-1} calculated for conduit parameters relevant to Enceladus, with a fluid transport timescale of $t \sim 500$ s (Nakajima & Ingersoll, 2016) between the liquid at T_{triple} (v_{fluid} = 5 m s^{-1}) and the surface vent at $T_{vent} \approx 200$ K (Goguen et al., 2013) (v_{fluid} = 150 m s^{-1}). The two classes of cooling rates result in different salt compositions and microscale spatial distributions (Thomas et al., 2019; Fox-Powell & Cousins, 2021). Such previously observed differences in

184 spatial distribution are likely not relevant at the macroscopic scales (centimeters) considered here,
185 which comprise all grains in a given section of the fluid path. However, we cannot exclude the
186 possibility that the formation of different salts affects salt-organic interactions (Vu et al., 2023),
187 and therefore, affects changes in the relative abundances of organic compounds.
188
189 We report the results of two sets of injections: one of a mixture of twelve amino acids
190 (three injections of the same volume of the same solution), and one of a mixture of two fatty acids
191 (two injections of different volumes of the same solution). All compounds were purchased from
192 Sigma-Aldrich (≥98% or higher purity) and used without further purification. The amino acids
193 listed in Table 1 were chosen to span compounds found only naturally on Earth in biological
194 samples (e.g., histidine), only in abiotic samples (e.g., 2-aminoisobutyic acid and γ-aminobutyric
195 acid), and in both types of samples (see Fig. 5 and references in its caption). The two fatty acids
196 were chosen as structural end-members: phenylacetic acid is a short aromatic compound, whereas
197 palmitic acid is a long aliphatic fatty acid commonly found in biological cellular membranes
198 (Madigan et al., 2012). The compounds were dissolved in deionized water (DI; 18.2 MΩ•cm)
199 containing 1 mass% NaCl (Sigma-Aldrich, ≥ 99%) and a sub-mass% amount of Na_2CO_3 to adjust
200 the pH to around 9. These salt composition and pH are intended to approximate the salt
201 composition and pH of Enceladus' ocean, inferred to be 0.5–2 mass% Na- and K- chloride and
202 carbonate (Postberg et al., 2011) and pH 8–10 (Glein & Waite, 2020; Fifer et al., 2022) based on
203 analyses of plume grains. These current best estimates are limited by the potentially biased
204 sampling by the Cassini spacecraft of only those plume grains that could reach sufficiently high
205 altitudes. Although ejected material has been best characterized at Enceladus, this composition is
206 broadly relevant to the NaCl and carbon-bearing deposits observed at, and deemed endogenic to,

Ceres, Europa, and Ganymede (De Sanctis et al., 2016; Trumbo et al., 2022; Villanueva et al., 2023b; Tosi et al., 2023). They do not encompass, e.g., $MgSO_4$-rich compositions that are part of possible compositions for Europa's ocean (e.g., Melwani Daswani et al., 2021).

Compound	Concentration (mM)	Solubility in H_2O at room temperature (mM)	pKa		
			–COOH	*–NH_2*	*Side chain*
Amino Acid Experiment (Volume 3x200 mL)					
Glycine (Gly)	2	3330.2	2.35	9.78	N/A
Alanine (Ala)	1	1000.1	2.35	9.87	N/A
Glutamic acid (Glu)	0.4	58.7	2.10	9.47	4.07
Aspartic acid (Asp)	0.4	31.6	1.99	9.90	3.90
Leucine (Leu)	1	175.3	2.33	9.74	N/A
Threonine (Thr)	0.6	719.4	2.09	9.10	N/A
2-aminoisobutyric acid (AIB)	2	1755.2	2.36	10.21	N/A
γ-aminoisobutyric acid (γAB)	2	998.8	4.53	10.22	N/A
Histidine (His)	1	277.2	1.80	9.33	6.04
Phenylalanine (Phe)	2	99.9	2.20	9.31	N/A
Tyrosine (Tyr)	0.2	2.6	2.20	9.21	10.46
Tryptophan (Trp)	0.1	64.6	2.46	9.41	N/A
Fatty Acid Experiment (Volumes 280 mL and 470 mL)					
Phenylacetic acid	8	110	N/A		
Palmitic acid	0.5	0.028	N/A		

Table 1. *Concentrations and properties of the amino and fatty acids injected into vacuum.*

Amino and fatty acid concentrations were on the order of mmol per kg H_2O (millimolar or mM). This is one to five orders of magnitude more concentrated than estimates for icy world subsurface oceans (e.g., Hand et al., 2016; Steel et al., 2017; Guzman et al., 2019; MacKenzie et al., 2022), but necessary to ensure detectable amounts of these organic compounds in compositional analyses (Sections 2.2 and 2.3). Millimolar concentrations are below saturation for all amino acids and phenylacetic acid, but above saturation for palmitic acid (Table 1), whose undissolved solid fraction could be seen suspended in solution, presumably as micelles, as well as

224 in clumps at the surface of the solution. The incomplete dissolution of palmitic acid did not affect
225 our ability to detect it in compositional analyses, but prevented quantification of exactly how much
226 palmitic acid was injected into vacuum. The suspended solids were injected, but the surface clumps
227 were not because the inlet of the injection line was dipped below the surface –and often near the
228 bottom– of the injected solutions.
229
230 After injection, the chamber was opened and the cup and supporting foil were stored inside
231 sterilized 50-mL polypropylene tubes. The injection line was taken apart and the dry residue,
232 presumably a mixture of salts and amino or fatty acids, was scraped and transferred using fine-
233 pointed tweezers or a metal spatula into separate polypropylene tubes for each section of the line:
234 (1) the two valves ("Valves"), (2) the flange attaching the injection line to the vacuum chamber
235 port ("Flange"), (3) the chamber port ("Port"), and (4) the collection cups and supporting foil
236 ("Chamber") (Fig. 2). In two pilot injections, the ice on the cold finger (Fig. 2a) was also recovered
237 by letting it melt inside a polypropylene tube. Although post-experiment reactivity of the samples
238 was not a concern, all tubes were sealed with Parafilm (not a contamination concern at the
239 relatively high organic concentrations of our experiments) and kept at room temperature at GSFC.
240 Sample tubes were shipped uncooled to Oakland University promptly after completion of the last
241 replicate experiment and received within six weeks of completion of the first replicate injection.
242 Thereafter, sample tubes were kept in a –20ºC freezer until the day of analysis.
243

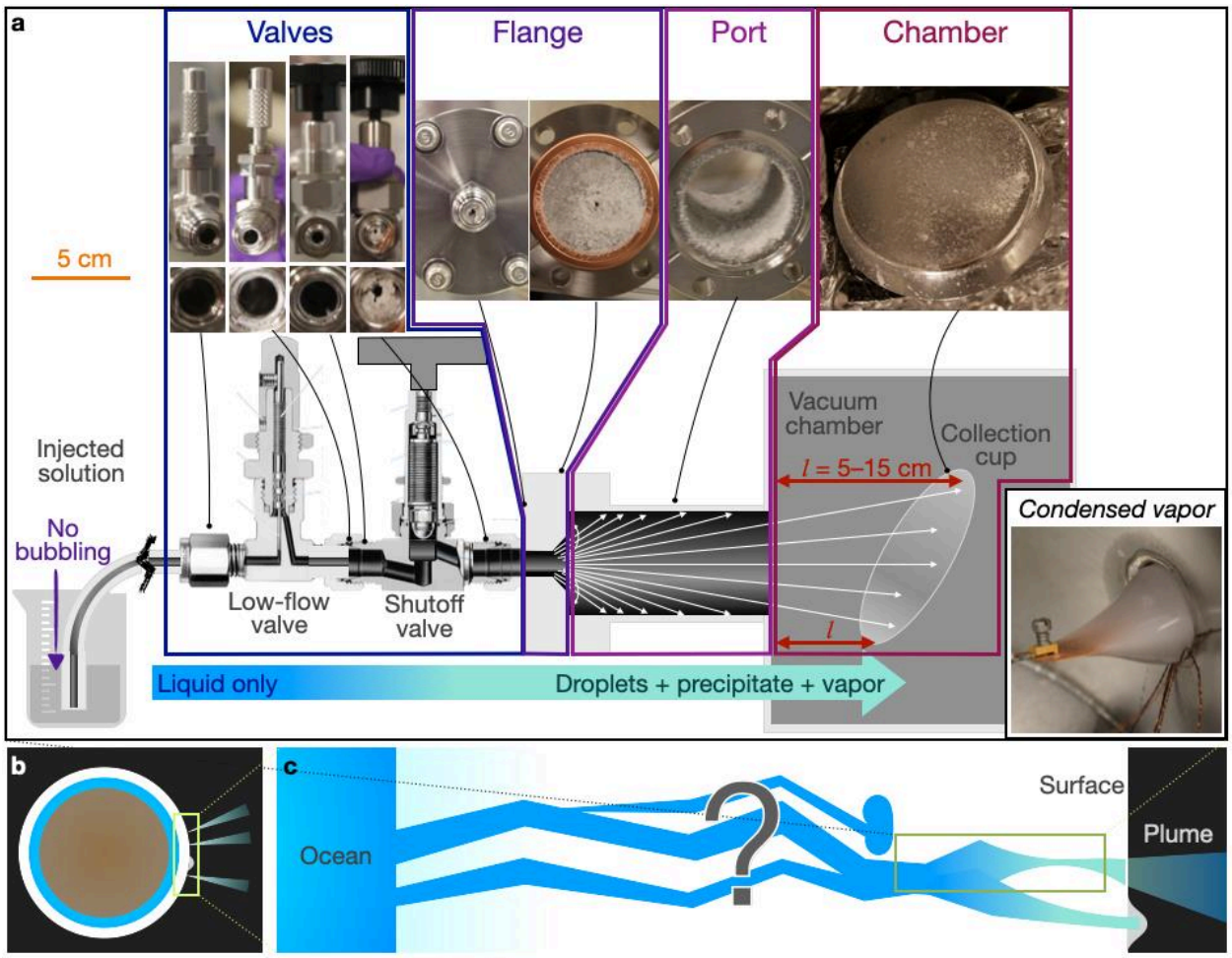

Figure 2. (a) *Cutaway, approximately to scale, of the injection line, showing the "valves", "flange", "port", and "chamber" sections in which dry residue was collected post-injection. Photographs taken during sample recovery point to corresponding locations in the line. The inset at bottom right shows vapor condensed as ice on the cryocooled copper plate inside the vacuum chamber, which could be recovered to measure its total organic carbon content.* ***(b)-(c)*** *Rough correspondence between the injection path and the liquid-vacuum transition undergone by ocean samples erupted on airless icy worlds. The question mark depicts the uncertainty on the nature of the conduit(s) bringing ocean material to the surface.*

256
257 *2.2. Amino Acids Analysis*
258
259 In the amino acid experiments, the collected samples were extracted using DI water
260 containing 10 mM phenol and 10 mM glutamine. Glutamine (≥99%), and phenol (99%) from
261 Sigma-Aldrich were used as internal standards for amino acid abundance quantification by high-
262 performance liquid chromatography (HPLC). DI water (18.2 MΩ•cm) was obtained from a
263 Barnstead Nanopure system. The potential salt effect on amino acid quantification was examined
264 by comparing measured abundances of amino acids at identical concentrations in solutions with
265 and without salt (e.g., 1% NaCl plus Na_2CO_3 to adjust the pH to 9.5). The differences observed in
266 retrieved abundances between the salted and unsalted samples on HPLC were < 5%, which is
267 generally less than the uncertainty among replicates (see Fig. 3). For the analysis of aromatic amino
268 acids (histidine, phenylalanine, tyrosine, and tryptophan), the samples were directly injected into
269 the HPLC without derivatization. For the analysis of the other eight non-aromatic amino acids, the
270 samples were derivatized following previous methods (Concha-Herrera et al., 2005; 2010).
271 Briefly, 2.50×10^{-2} M of o-phthaldialdehyde (OPA) and 5.0×10^{-2} M of N-acetylcysteine (NAC)
272 were prepared in a 1 M boric acid buffer solution (pH 9.5) as the derivatization reagent. The
273 mixture was protected from light with aluminum foil, stored at 4ºC, and prepared on a weekly
274 basis to avoid degradation. An aliquot of 50 µL of the amino acid sample solution was mixed with
275 500 µL of the derivatization reagent for a 10-min reaction prior to the HPLC analysis. NAC
276 (≥99%), OPA (≥97%), and NaOH (98%) were purchased from Sigma-Aldrich; boric acid (≥99%)
277 was purchased from Alfa-Aesar.
278
279 The HPLC (PerkinElmer 200 series) is equipped with a Flexar binary pump, a Shim-pack
280 CLC-C18 column (Shimadzu), and a UV-Vis detector. The mobile phases include a citric acid

buffer (A) at pH 6.5±0.1 and acetonitrile (B) (HPLC-grade). Two different mobile phase programs were used for underivatized and derivatized samples. For underivatized amino acids, the mobile phase composition was programmed to start at 100%A (3 min), to 80%A and 20%B (3 min), to 78%A and 22%B (4 min), to 70%A and 30%B (6 min), followed by another hold for 2 min. The mobile phase flow rate was 1.00 mL min^{-1} and the UV detection wavelength was at 225 nm. For the derivatized amino acids, the mobile phase composition was programmed to start at 100%A (1 min), to 97%A and 3%B (2 min), to 90%A and 10%B (10 min), to 80%A and 20%B (20 min), to 75%A and 25%B (6 min) and hold for another minute. The mobile phase flow rate was also 1.00 mL min^{-1} and the UV detection wavelength was at 335 nm. For both methods, 50 µL of sample was injected with a 20 µL sample loop.

2.3. Fatty Acids Analysis

In the fatty acid experiments, the samples were first acidified using HCl to ensure the carboxylates were protonated and fully extractable by the organic solvent. The samples were then extracted with dichloromethane (DCM, VWR, 99.9%), vortexed, and centrifuged to separate the organic layer from the aqueous layer following previous procedures (Fu et al., 2020a; Aspin et al., 2023). The aqueous layer was additionally washed twice with DCM, and the DCM extract was combined with the previous organic layer to ensure sufficient extraction. The separation of DCM extract from the aqueous phase also removed the sodium salts (e.g., NaCl and Na_2CO_3) from the protonated fatty acids prior to the gas chromatography (GC) analysis. After evaporating DCM at room temperature, the solid lipids were redissolved in a 0.5 mL DCM solution containing 0.88 mM decane (Sigma-Aldrich, ≥99%) as the internal standard for GC quantifications (Fu et al., 2020b; Liao et al., 2022).

304

305 The GC (Agilent 7820A) is equipped with a poly-capillary column, an autosampler, and a
306 flame-ionization detector. Helium was used as the carrier gas, and the GC oven was programmed
307 to initiate at 50ºC for 8 min, ramp at 10ºC min^{-1} up to 220ºC, hold for 10 min, ramp at 20ºC min^{-1}
308 to reach 300ºC for 5 min. The injection temperature was at 275ºC, and the detector temperature
309 was set to 300ºC with air flow at 400 mL min^{-1}, H_2 flow at 30 mL min^{-1}, and N_2 flow at 25 mL
310 min^{-1}.

311 **3. Results**

312
313 Dry residue was recovered not only inside the vacuum chamber (cups and foil), but also in
314 the chamber port, its cover flange, the shutoff valve (Fig. 2), and in some injections, as far upstream
315 as between the low-flow and shutoff valves. Most of the residue coated the inner surfaces of the
316 port and flange, due presumably to a combination of (a) low pressure favoring water loss and solute
317 precipitation, (b) high area for deposition, and (c) a cross-sectional area small enough relative to
318 the port length to allow the flow to interact extensively with the port wall. Further upstream, the
319 line's lower cross-sectional area limited the surface area available for deposition (Fig. 2). During
320 injections, precipitate intermittently clogged the line, as evidenced by spontaneous decreases in
321 the injection rate (change in remaining solution volume as a function of time), episodic pressure
322 spikes from the baseline H_2O vapor pressure at the copper plate temperature, and occasional
323 observations of collection cup deflections upon grain impact when increasing the injection flow
324 rate (Supplementary video) concurrent with precipitate accumulation in the cup. The size of
325 residue grains could only be reliably verified in the collection cup where, unlike in the injection
326 line, the surface was not uniformly coated, allowing observation of individual grains. Sizes were

not quantified, but macroscopic inspection (e.g., Fig. 2a) confirmed that residue grains had sub-millimeter sizes, presumably extending down to microscopic (Section 2).

Aside from a negligible fraction of carbonate salt converted to CO_2 at pH > 9, all solutes are less volatile than H_2O (Section 4). The vapor condensed onto the copper plate cold finger during two pilot injections indeed had a total organic carbon content of < 0.015% and < 0.001% of that of the injected solution.

3.1. Amino acid fractionation

The total mass of each amino acid in all four sections of the flow path was 60% to 120% of their masses in the injected solution, with a recovery of 80 to 110 mass% for most (Fig. 3a). The highest measured recoveries are compatible with 100% within two standard deviations from the mean of three replicate injections. We ascribe the measurement uncertainty to variations in sample collection, extraction, dilution, and/or quantification among replicates. Four amino acids had low recovery, more than two standard deviations away from 100%: Asp, AIB, Tyr, and Trp (Fig. 3a). Three of those have relatively low solubility in water (Table 1, see also Fig. 7a), which might account for some of the losses (e.g., material remaining inside valves or not transferred across steps of the preparation for analysis).

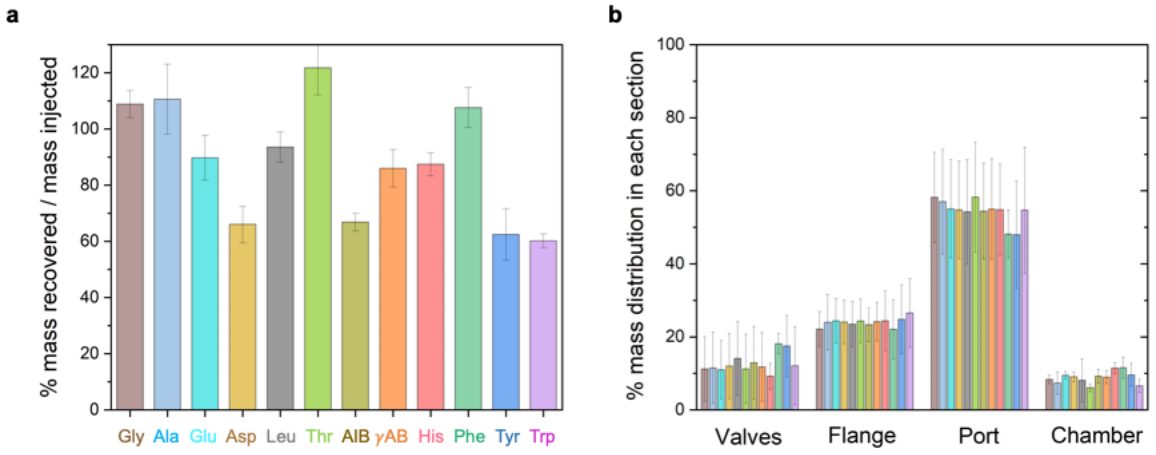

Figure 3. (a) *Total recovery (mass%) of each amino acid in all four sections of the injection path (outlined in Fig. 2a).* ***(b)*** *Distribution (mass% of total amino acids in (a)) in each section. Error bars indicate one standard deviation from the mean of three replicate injections.*

The amount of deposited amino acids increased downstream (Fig. 3b) from the valves (10–20% of the mass of each amino acid collected post-injection), through the flange (22–26%), to the port (50–60%), consistently with the amounts of residue recovered (Fig. 2), and with the caveat that the uncertainties on recoveries from the valves and flange sections overlap. In most cases, there was no difference among amino acids within one standard deviation uncertainty. Only 6–12% reached the vacuum chamber.

3.2. Fatty acid fractionation

Distributions of fatty acids along the injection path were similar: most of the mass was collected in the main port, and a few percent in the chamber (Fig. 4a). The total mass of phenylacetic acid recovered in all four sections was 81% of the mass injected, which is consistent with an empirically determined ≈85% efficiency of the lipid extraction method (Section 2). However, the total mass of palmitic acid recovered was only 9.9% of the mass that should have

been injected with palmitic acid fully dissolved. This low recovery is likely due in part to the incomplete injection of palmitic acid, which was supersaturated in the injected solution, and in part due to analytical uncertainties arising from recovered palmitic acid amounts (0.1 to 0.8 mg across all flow sections) close to the limit of detection (0.14 mg).

Notwithstanding this systematic uncertainty in palmitic acid abundance determination, we observed a striking change in the relative abundance (mass ratio) of phenylacetic acid to palmitic acid in the downstream direction of the flow. This mass ratio was 45 at the valves, increasing to 132 at the flange and 301 in the port (Fig. 4b). The ratio in the injected solution is expected to be higher than 8 (had all palmitic acid fully dissolved) and 152 or less (had only palmitic acid dissolved up to saturation been injected, excluding suspended micelles). The upper limit is broadly consistent with the recovered mass ratio in the chamber (182) and summed over all four sections (201) given the uncertain palmitic acid abundance determinations.

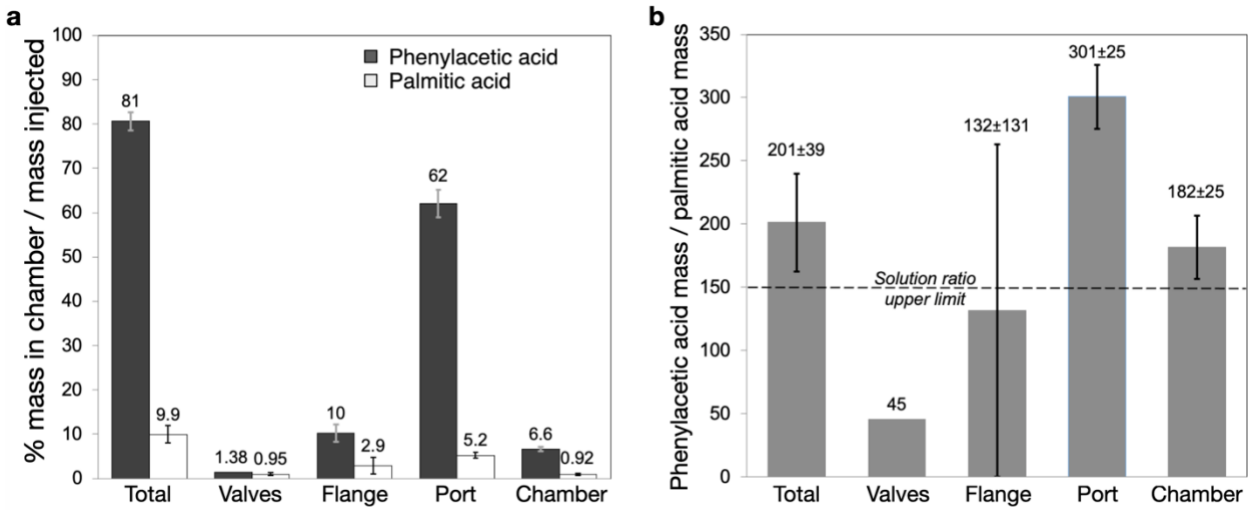

Figure 4. (a) *Mass fraction (%) of fatty acids recovered in sections of the injection path relative to the dry mass added to water when preparing the solution for injection.* ***(b)*** *Mass ratio of phenylacetic acid to palmitic acid in each section of the injection path. Error bars indicate one*

standard deviation (volume-weighted) from the volume-weighted mean of two injections of 280 mL and 470 mL of the same solution.

4. Discussion

4.1. Interpretation of relative abundance measurements by spacecraft

The observed limited amino acid abundance fractionation is sensible in that amino acids have limited volatility relative to water. They are also very soluble in water, with which they primarily interact via the amine and carboxyl functional groups that drive the aqueous behavior of all amino acid compounds investigated here. This suggests a low propensity for selectively coming out of solution as either solid or vapor, even at the high end of conduit temperatures (> 250 K), confirmed by the present experiments.

The changes in relative amino acid abundances between the injected solution and the vacuum environment (chamber; last group of Fig. 3b), shown in Fig. 5b, do not appear to affect the relative distributions of amino acids in example biological and abiotic samples (Fig. 5a) in ways that prevent distinction between these two representative end-member sources (Fig. 5c). Barring fractionation processes not produced by our experimental procedure, the proportions of amino acids in material having undergone the liquid-vacuum transition during eruption should be as indicative of their origin as those in the subsurface liquid source. Thus, measurements of amino acid relative abundances by spacecraft that would analyze macroscopic samples (homogenizing grain-to-grain differences) of material having undergone the liquid-vacuum transition during eruption on Europa (Hand et al., 2022) and Enceladus (MacKenzie et al., 2022) should be able to distinguish biological from abiotic end-member sources for these compounds without needing to

correct for abundance fractionations arising from this environmental transition. Interpretation of such measurements may need to consider additional processes that could cause abundance fractionations, such as space weathering (e.g., irradiation), any possible biases introduced by the sampling altitude or surface location, or the possibility of mixing with material encountered on the way to the surface.

Whether the liquid-to-vacuum transition changes the relative abundances of fatty acids is less clear. The mass ratio of phenylacetic acid to palmitic acid in the vacuum chamber (182±25), may be close to the ratio injected (152, if the palmitic acid injected was only that dissolved to saturation in the parent solution). However, the injected ratio would have been as low as 8.4, had all palmitic acid particulates (suspended and floating) been injected as well. While the suspended material was likely injected, the clumpy floating material was not. This floating material comprised an estimated 87 mg of the 129 mg added during solution preparation (67 mass%), so the injected ratio was likely $\geq 8.4 / (1 - 87/129) = 26$ and the mass ratio likely did not change by a factor higher than $(182 \pm 25)/26 = 7 \pm 1$.

A factor-of-7 or lesser change in relative abundances could alter patterns arising from relevant example biological and abiotic sources, but likely not so much as to make them unrecognizable. Abiotic straight-chain fatty acids (alkanoic acids) formed in water from formic acid (an expected conversion product of accreted carbon monoxide (Shock, 1993; Neveu et al., 2015)) have relative abundances that track those of straight-chained alkanes (McCollom et al., 1999), which themselves decrease monotonically by a factor of 3 between C_n- and C_{n+4}-compounds comprising $n = 10$ to 24 carbon atoms (McCollom & Seewald, 2006). In microorganisms, alkanoic

435 acid abundances peak at specific carbon numbers (Hamerly et al., 2015), with abundance ratios of
436 2 to 10 between alkanoic acids differing by one carbon atom in their chain lengths (Bühring et al.,
437 2005). Thus, a factor of $\leq 7\pm1$ change in the relative abundances of alkanoic acids differing by a
438 few carbon atoms in their chain length would complicate recognition of an abiotic or biological
439 source from abundance patterns (Hand et al., 2016; MacKenzie et al., 2022). However, the liquid-
440 vacuum transition would likely cause a much smaller change, as there are much less structural
441 differences between these compounds than between the phenylacetic acid (a short-chain aromatic
442 acid) and palmitic acid (C_{16} alkanoic acid) investigated here.
443

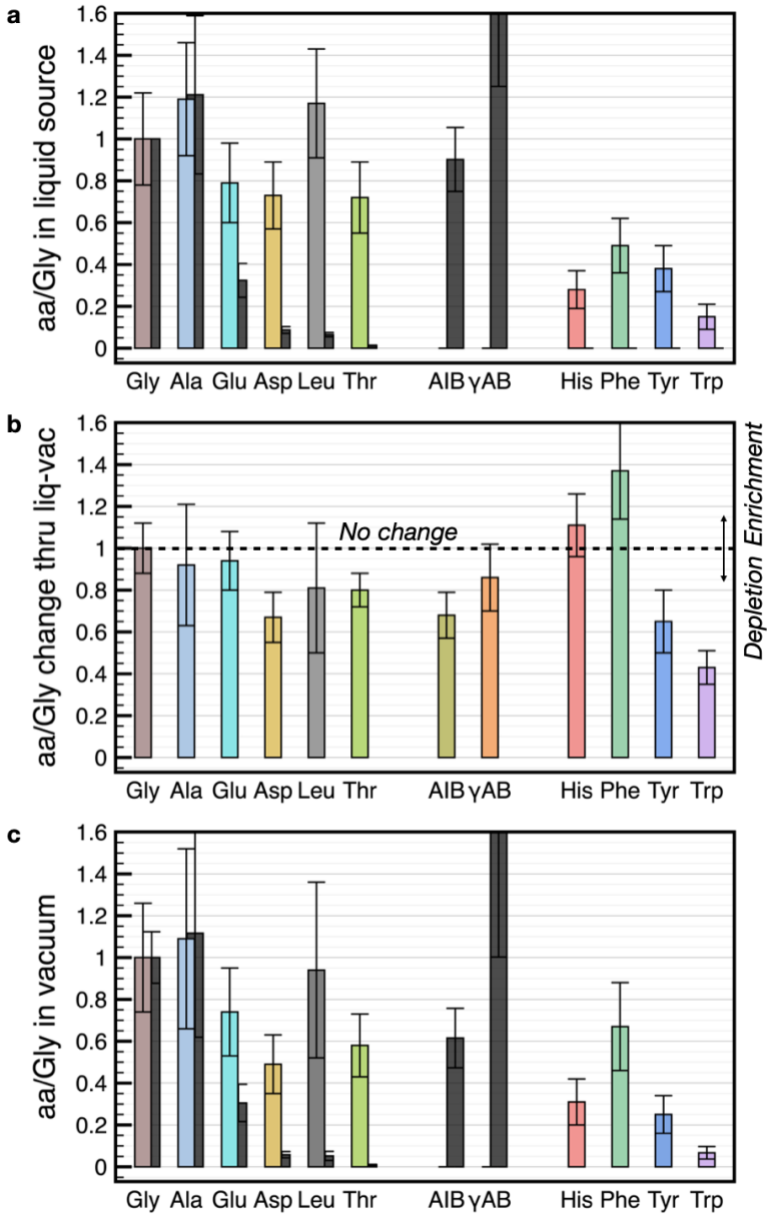

Figure 5. (a) *Example biological (colored bars) and abiotic (shifted dark bars just to the right of the colored bars) mass ratios of amino acids to glycine ("aa/Gly") for the twelve amino acids injected. The abiotic γAB:Gly ratio is 2.5±1.3 (off scale).* ***(b)*** *Ratio of Chamber aa/Gly to injected solution aa/Gly for these amino acids. A ratio higher or smaller than 1 indicates, respectively, enrichment or depletion of the corresponding amino acid relative to Gly in vacuum.* ***(c)*** *Same distributions as in (a) but multiplied by the ratios in (b) to show predicted relative amino acid*

abundances in ejected material with initially example biological or abiotic end-member amino acid abundance distributions. The abiotic γAB:Gly ratio is 2.2±1.2 (off scale).

Notes: In (a), example biological aa/Gly are the average of data from Nishikawa & Ooi (1982) for 356 proteins with molecular mass > 5000 Da from prokaryotes and eukaryotes, and from Lobry & Gautier (1994) for E. coli*; both datasets have very similar values. Uncertainties are the square root of the sum of the two squared uncertainties, divided by √2. Abiotic aa/Gly are the average of (total hydrolyzed amino acid)/(total hydrolyzed Gly) in up to eleven measurements: Ryugu samples A0106 (one measurement from Naraoka et al., 2023; one from Parker et al., 2023) and C0107 (Parker et al., 2023); CM chondrites Winchcombe (Chan et al., 2023) and Asuka 12236 (Glavin et al., 2020); and CR chondrites GRO 95577, EET 92042, and QUE99177 (Glavin et al., 2010), MIL 090001 and MIL 090657 (Aponte et al., 2020), and GRA 95229 (Martins et al., 2007). Abundances for which the L-enantiomer was more abundant than the D-enantiomer above 1 sigma were ignored to screen out potential terrestrial contamination. Uncertainties are standard errors among the samples for which aa/Gly was reported and had no such L-excess; uncertainties reported for individual measurements were not propagated.*

Amino and fatty acid distributions may well result from a mixture of biological and abiotic end-member sources, but the ability to discern individual source contributions to abundance patterns appears not to be affected much by abundance changes induced by the liquid-vacuum transition. Interpretation of Fig. 5c suggests that example biological and abiotic sources would remain identifiable through the presence of amino acids that are not observed in the other end member, such as the right-most six amino acids in Fig. 5. Regarding fatty acid abundance patterns, as shown in Fig. 6a and 6b, respectively, the dominant modeled example biological (even over odd) or abiotic contribution (decrease with increasing carbon number) to the pattern remains qualitatively identifiable even if the minor contributor accounts for 20% of the signal, assuming

the liquid-vacuum transition induces a –likely overestimated– random factor-of-7 change in abundances. In a mixture where modeled biological and abiotic contributions are equal (Fig. 6c), the modeled abundance patterns remain qualitatively faintly identifiable, but only if the liquid-vacuum transition changes abundances by a random factor of ≤ 2.

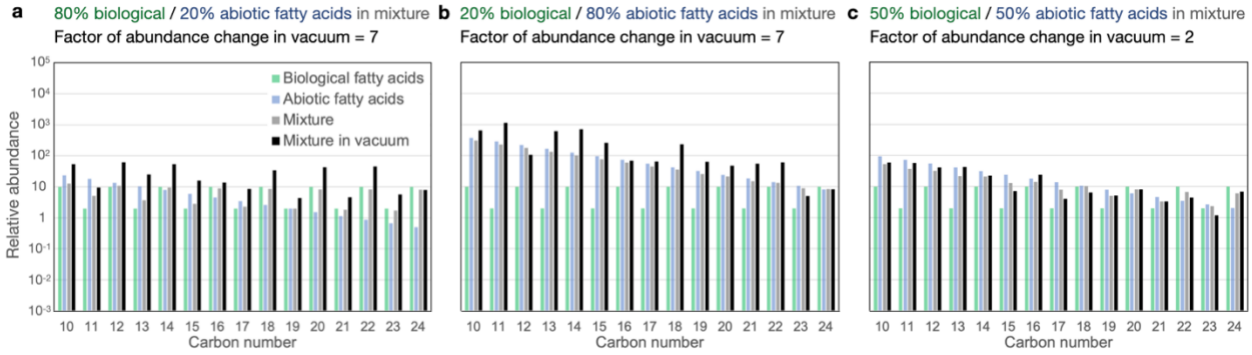

Figure 6. *Modeled relative abundance patterns of a mixture of fatty acids deriving from idealized biological and abiotic sources. The modeled biological source (green histograms) has an arbitrary abundance of 10 for alkanoic acids with odd carbon numbers and 2 for those with even carbon numbers (even/odd abundance ratio = 5). The modeled abiotic source (blue histograms) has abundances decreasing by a factor of $3^{1/4}$ between adjacent carbon numbers. The mixture (grey histograms) is the sum of the two. The effect of the liquid-vacuum transition is modeled as a random change in abundances by an arbitrary factor (black histograms).* ***(a)*** *Mixture of 80% biological / 20% abiotic pattern, with a factor-of-7 random abundance change induced by the liquid-vacuum transition.* ***(b)*** *Mixture of 20% biological / 80% abiotic pattern, with a factor-of-7 random abundance change.* ***(c)*** *50% / 50% mixture, with a factor-of-2 random abundance change.*

4.2. Possible causes for relative abundance changes

Despite overall preservation of amino and fatty acid mass ratios at scales relevant to identifying their source, the liquid-vacuum transition causes up to 50% changes in the mass ratios of amino acids and possibly larger changes in those of phenylacetic and palmitic acid. Below, we investigate possible causes for these changes, arising either from intrinsic physicochemical properties of these compounds or from the experimental procedure. Among these, solubility –and, relatedly, flow rate– appear to have the most effect. While other properties could sensibly fractionate compound abundances, no strong effects of these were observed.

4.2.1. Solubility

The abundant precipitate formed along the fluid path (Fig. 2 and 3b), as water is lost to vaporization, suggests that compound solubilities could affect their relative abundances in the chamber. The mass of amino acids in the collection chamber shows a weak increasing correlation with compound solubility (Fig. 7a) and injected concentration (Fig. 7b). Considering additionally the fatty acid experiment and pilot, singleton injections of amino and fatty acids, compound depletion through the liquid-vacuum transition generally decreases with increasing concentration:solubility ratio (Fig. 7c). Lesser saturation may increase the retention of amino and fatty acids in the aqueous phase, thus increasing their propensity for reaching the vacuum environment.

Irrespective of compound solubility, most of the dry residue was recovered from the "Port" section partway through the fluid path (Fig. 2 and 3b), rather than inside the chamber. This is in part due to the Port's significant surface area (65 cm^2), equivalent to the material deposition area inside the chamber (≈ 60 cm^2 for two collection cups plus part of the support foil; Fig. 1b). Scaling Fig. 3b and 4a to the estimated surface area of deposition for each section (≈ 18 cm^2 for the Flange,

≈ 5 cm^2 for the Valves), most relative areal mass densities of compounds decrease monotonically in more downstream sections (Fig. 7d).

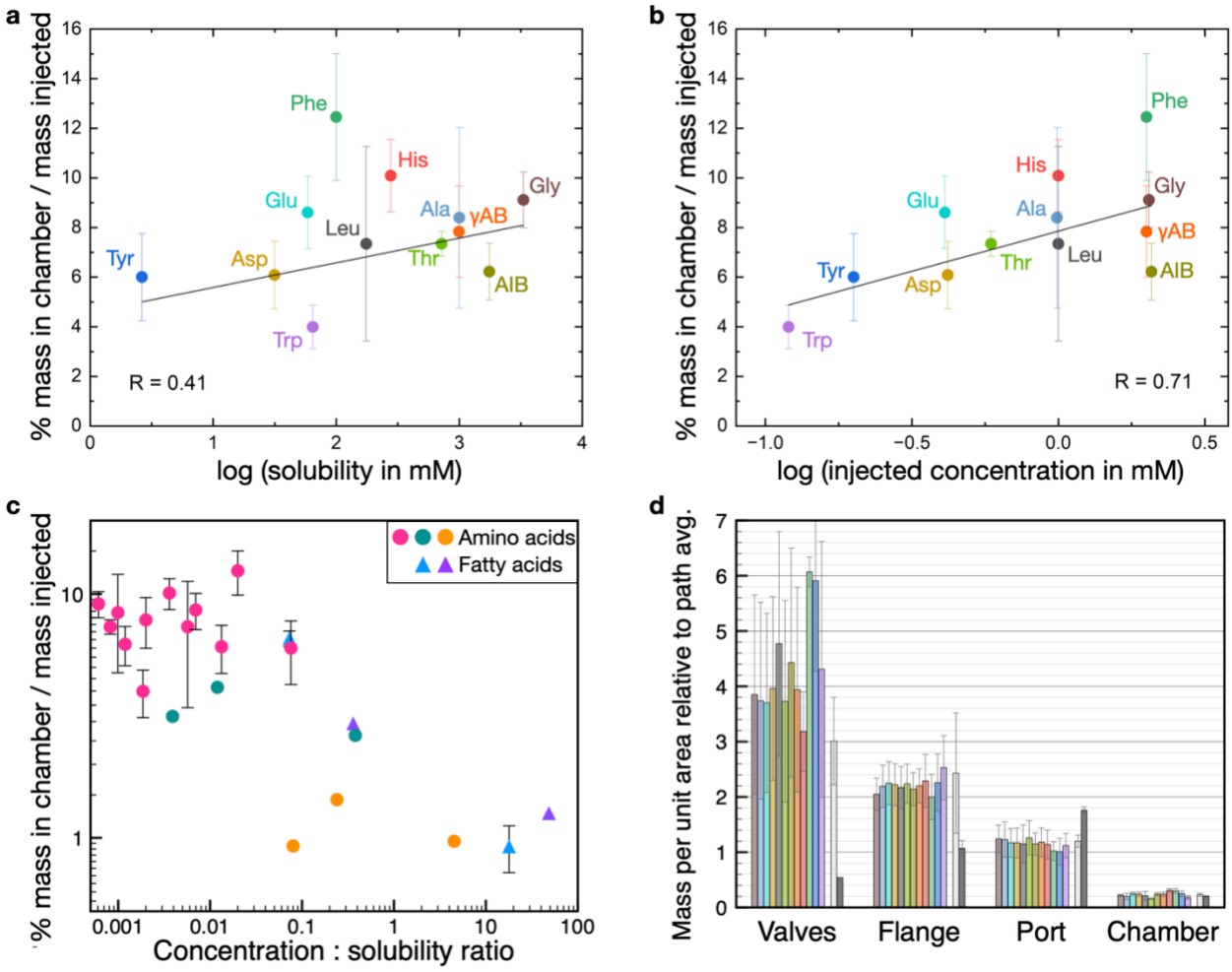

Figure 7. *Solubility effect on the propensity of amino and fatty acids for transport through the liquid-vacuum transition.* ***(a)*** *and* ***(b)*** *Mass percent of each amino acid in the collection chamber as a function of, respectively, its solubility or injected concentration. Error bars indicate one standard deviation from the mean of three replicate injections.* ***(c)*** *Mass percent of amino and fatty acids, aggregated across experiments, as a function of the ratio of their concentration in the injected solution to their solubility. Circles denote amino acids (pink for the experiment reported here, teal and orange for two pilot singleton injections); triangles denote fatty acids (blue for the*

experiment reported here, purple for one pilot singleton injection). Error bars indicate one standard deviation from the mean of three or two replicate injections (pink or blue data points, respectively). ***(d)*** *Areal mass density of organic acid (color-coded as in Fig. 3b and 4a) per section of the injection path, relative to the areal mass density averaged across the full injection path. Error bars indicate uncertainty propagated from one standard error from the mean of three or two replicate injections (amino or fatty acids, respectively). For the fatty acids in (d), the standard error is the volume-weighted standard deviation from the volume-weighted mean, divided by √2.*

On icy moons, expected amino and fatty acid concentrations in the subsurface ocean are much lower (sub-micromolar; Section 2) than in the millimolar solutions we injected. Lower concentrations may lessen the effect of solubility on relative abundance fractionation for these compounds. So, too, may the lower temperatures of eruption conduits relative to the 30ºC±15ºC of our injection line (Section 2.1), because less water would be lost from the condensed phase. However, for more concentrated and possibly less soluble compounds such as those observed and inferred to be sourced from subsurface liquid water at Enceladus (~0.03 mM; Postberg et al., 2018a; MacKenzie et al., 2022) and Ceres (percent-level abundances in surface materials; Kaplan et al., 2018; Daly et al., 2023), precipitation could both coat the eruption conduit walls with precipitate whose solubility decreases with increasing depth and skew relative abundances in materials exposed to vacuum during eruption.

4.2.2. Volatility

Vaporization or sublimation of amino and fatty acids is an improbable cause of abundance fractionation. First, the total organic content measured in vapor condensed inside the vacuum chamber was negligible. Second, amino and fatty acids are less volatile than water: although –to

our knowledge– unreported, their vapor pressures should be lower, and their triple points at higher temperature and pressure, than those of smaller acetic acid (CH_3COOH), whose vapor pressure is itself lower, and triple point higher, than those of H_2O (NIST, 2023, and references therein).

4.2.3. Charge and organic-salt interactions

The respective pH of the injected amino and fatty acid solutions were 9.2 and 9.7. At pH 9.2, the carboxyl groups of the amino acids are deprotonated (COO^-) because of their low *p*Ka values (1.8–2.4), whereas the amine groups could be protonated (NH_3^+; *p*Ka 9.1–10.5). Amino acids Asp, Glu, His, and Tyr also have pH-sensitive side chains with *p*Ka 3.9–10.4. At pH 9.7, phenylacetic acid and palmitic acid too were present as their carboxylates (*p*Ka 4.31 and 4.95, respectively). The COO^- groups of amino and fatty acids likely interact with the Na^+ in solution; protonated amine groups and charged side chains could also affect ionic interactions with the salts.

Such organic-salt interactions can fractionate relative abundances of lipids at liquid water-gas interfaces (Cochran et al., 2016), and co-locate glycine and (more strongly) aspartic acid with salts in frozen brines of sodium chloride and carbonate, particularly with sodium carbonate due its higher charge density (Vu et al., 2023). Because salts are in large excess (mass%-level) both in our experiments and in relevant icy world environments (Postberg et al., 2011; Castillo-Rogez et al., 2018; Melwani Daswani et al., 2021) relative to amino and fatty acids, partial precipitation of salts along the liquid-vacuum path could induce co-precipitation of these organic acids that can fractionate their relative abundances. We measured no significant effect on the ratio of {mass in chamber} to {mass injected} between overall negatively charged Tyr, Asp, Glu, and Thr and the other, overall electrically neutral amino acids (Fig. S1), suggesting no detectable effect of organic-salt interactions on abundance fractionations at this macroscopic scale. However, we cannot

583 exclude that the possibly different organic-salt interactions resulting from the expected cooling
584 rates at Enceladus, which are likely to be much lower than those of our experiments (Section 2.1),
585 could fractionate amino acids depending on their electrical charge.

586
587 *4.2.4. Chemical structure and functionality*
588
589 The investigated amino acids consist of both aromatic and non-aromatic structures, some
590 more electrically polar and others more hydrophobic (Bull & Breese, 1974). Studies of aerosol
591 formation from aqueous solutions (e.g., seawater) have shown that amino acids could affect
592 aerosol properties such as surface tension, surface activity, hygroscopicity, and potential surface
593 reactions (Herboth et al., 2021; Marsh et al., 2017), and that pH can play an important role in the
594 amino acid distribution in aerosols. For example, hydrophilic amino acids such as Gly tend to be
595 distributed in the bulk of aerosol droplets, whereas amphiphilic and hydrophobic amino acids such
596 as Ala and Phe tend to be located on droplet surfaces. Although the aerosol studies were carried
597 out at 1 bar, the chemical properties of amino acids may also shape patterns of distribution at solid-
598 liquid-vapor interfaces at the sub-P_t regime investigated here.

599

600 However, these properties do not appear to affect the ratio of {mass in chamber} to {mass
601 injected} for specific amino acids (Fig. S2 and S3). The polar-basic His, as well as Gly, have a
602 slightly higher ratio than the polar-neutral Thr, but the effect is small. If chemical structure and
603 functionality influence the ability of organic compounds in solution to be transported to vacuum
604 environments in water droplets or grains, this influence appears to be similar among compounds
605 that all have in common carboxyl and amine functional groups.

606
607 *4.2.5. Flow rate*
608

609 As observed during experiments, higher fluid flow rates can move more solutes along the
610 fluid path by limiting the gradual loss of water and can mechanically dislodge prior precipitate.
611 Despite the use of a low-flow valve, flow rate was only coarsely controlled during the injection
612 experiments because precipitation tended to effectively decrease conduit diameters in a way that
613 could be neither quantified nor adjusted. Thus, the flow rate could vary across the full practical 1–
614 25 mL h^{-1} range during individual experiments.
615
616 The effect of such variable flow rates on the distributions of organic precipitate along the
617 fluid path may be captured by replicate-to-replicate differences in these distributions (error bars in
618 Fig. 3, 4, 5b, and 6; standard deviations in Table S1). These variations were generally a few percent
619 of the injected mass of each compound. Variations relative to the amount of material deposited in
620 each section of the injection path were about 20–65%. The highest relative variations were in the
621 valves, which are both the farthest (highest-pressure) section from the vacuum chamber and the
622 section with the lowest volume and surface area, i.e., the most sensitive to variations in flow rate.
623 The lowest relative variations were in the chamber port, where the most material was deposited.
624
625 Flow rate thus likely acts in combination with solubility to affect the distribution of organic
626 precipitate along the fluid path, both in these experiments and in eruption conduits at ocean worlds.
627 We suspect that the effects of solubility discussed above are increasingly pronounced at lower flow
628 rates. In addition to flow rate, other factors such as salt content may also influence the solubility
629 of organic acids, especially for those with low solubility (e.g., palmitic acid). Future experiments
630 with varying salt composition and concentration are needed to identify other drivers for changing
631 relative abundances of biosignature compounds in cryovolcanic ocean worlds.

5. Conclusions

The liquid-vacuum transition does not appear to alter relative abundances of amino and fatty acids enough to prevent distinction between end-member example biological or abiotic sources. Measured changes in relative abundances are primarily attributed to differences in compound concentrations in relation to their solubility in water, but these changes are only significant over a wide range of concentration:solubility ratios. Their importance may be modulated by the fluid flow rate, and may be lower at ocean worlds where amino and fatty acid abundances are expected to be orders of magnitude more diluted than in the present experiments. Thus, barring fractionation processes not produced by our experimental procedure, the proportions of amino and fatty acids in erupted material –measurable by spacecraft– having undergone the liquid-vacuum transition should broadly reflect those in the subsurface liquid source.

Acknowledgements

We thank two anonymous reviewers whose comments greatly improved this manuscript. This work was funded by a Scialog program (Signatures of Life in the Universe) sponsored jointly by the Research Corporation for Science Advancement, Heising-Simons Foundation, and Kavli Foundation (via award #28134 to Oakland University by RCSA), and by NASA's Fundamental Laboratory Research (Internal Scientist Funding Model) via award # 80GSFC21M0002 (CRESST-II agreement between NASA Goddard Space Flight Center and the University of Maryland, College Park). M.N. thanks M.G. Noreiga and V.M. Outsa for support in respectively machining the copper plate and connecting its temperature sensor for cryocooling. Z.Y. thanks D. Love for assistance in HPLC setup and configuration.

References

Aponte, J.C., Elsila, J.E., Hein, J.E., Dworkin, J.P., Glavin, D.P., McLain, H.L., Parker, E.T., Cao, T., Berger, E.L. and Burton, A.S., 2020. Analysis of amino acids, hydroxy acids, and amines in CR chondrites. Meteoritics & Planetary Science 55, 2422-2439. https://doi.org/10.1111/maps.13586.

Aspin, A., Smith, B., Burcar, E., Firestone, Z., and Yang, Z., 2023. Experimental and theoretical investigation of alkene transformations in oceanic hydrothermal fluids: A mechanistic study of styrene. Geophysical Research Letters 50, e2023GL103738. https://doi.org/10.1029/2023GL103738.

Bouquet, A., Glein, C.R. and Waite, J.H., 2019. How adsorption affects the gas–ice partitioning of organics erupted from Enceladus. The Astrophysical Journal 873, 28. https://doi.org/10.3847/1538-4357/ab0100.

Bühring, S.I., Elvert, M. and Witte, U., 2005. The microbial community structure of different permeable sandy sediments characterized by the investigation of bacterial fatty acids and fluorescence in situ hybridization. Environmental microbiology 7, 281-293. https://doi.org/10.1111/j.1462-2920.2004.00710.x.

Bull, H.B.; Breese, K., 1974 Surface Tension of Amino Acid Solutions: A Hydrophobicity Scale of the Amino Acid Residues. Arch. Biochem. Biophys. 161, 665–670. https://doi.org/10.1016/0003-9861(74)90352-X.

Cable, M.L., Neveu, M., Hsu, H.W. and Hoehler, T.M., 2020. Enceladus, in: Meadows, V., Arney, G., Schmidt, B., Des Marais, D.J. (Eds.), Planetary Astrobiology. University of Arizona Press, Tucson, pp. 217-246. https://doi.org/10.2458/azu_uapress_9780816540068.

Cable, M.L., Porco, C., Glein, C.R., German, C.R., MacKenzie, S.M., Neveu, M., Hoehler, T.M., Hofmann, A.E., Hendrix, A.R., Eigenbrode, J., Postberg, F., et al., 2021. The science case for a return to Enceladus. The Planetary Science Journal, 2, 132. https://doi.org/10.3847/PSJ/abfb7a.

Castillo-Rogez, J., Neveu, M., McSween, H.Y., Fu, R.R., Toplis, M.J. and Prettyman, T., 2018. Insights into Ceres's evolution from surface composition. Meteoritics & Planetary Science 53, 1820-1843. https://doi.org/10.1111/maps.13181.

Chan, Q.H., Watson, J.S., Sephton, M.A., O'Brien, Á.C. and Hallis, L.J., 2023. The amino acid and polycyclic aromatic hydrocarbon compositions of the promptly recovered CM2 Winchcombe carbonaceous chondrite. Meteoritics & Planetary Science, 1-30. https://doi.org/10.1111/maps.13936.

Cochran, R.E., Jayarathne, T., Stone, E.A. and Grassian, V.H., 2016. Selectivity across the interface: A test of surface activity in the composition of organic-enriched aerosols from bubble bursting. The Journal of Physical Chemistry Letters 7, 1692-1696. https://doi.org/10.1021/acs.jpclett.6b00489.

Concha-Herrera, V., Lerma-García, M. J., Herrero-Martínez, J. M. and Simó-Alfonso, E. F., 2010. Classification of Vegetable Oils According to Their Botanical Origin Using Amino Acid Profiles Established by High Performance Liquid Chromatography with UV–Vis Detection: A First Approach. Food Chem. 120, 1149–1154. https://doi.org/10.1016/j.foodchem.2009.11.046.

Concha-Herrera, V., Vivó-Truyols, G., Torres-Lapasió, J. R. and García-Alvarez-Coque, M. C., 2005. Limits of Multi-Linear Gradient Optimisation in Reversed-Phase Liquid Chromatography. J. Chromatogr. A 1063, 79–88. https://doi.org/10.1016/j.chroma.2004.12.001.

Daly, R.T., Rentas Marchand, A.N., Pontefract, A., Stockstill-Cahill, K.R., Martin, A.C., Sunshine, J.M., Mayorga, L.C., and Rizos, J.L., 2023. The effects of impacts on the reflectance spectra of aliphatic organics: Implications for Ceres. Geological Society of America Annual Scientific Meeting, Abstract 153-1. https://gsa.confex.com/gsa/2023AM/meetingapp.cgi/Paper/392730.

De Sanctis, M.C., Raponi, A., Ammannito, E., Ciarniello, M., Toplis, M.J., McSween, H.Y., Castillo-Rogez, J.C., Ehlmann, B.L., Carrozzo, F.G., Marchi, S., Tosi, F., et al., 2016. Bright carbonate deposits as evidence of aqueous alteration on (1) Ceres. Nature 536, 54-57. https://doi.org/10.1038/nature18290.

Dorn, E.D., McDonald, G.D., Storrie-Lombardi, M.C. and Nealson, K.H., 2003. Principal component analysis and neural networks for detection of amino acid biosignatures. Icarus 166, 403-409. https://doi.org/10.1016/j.icarus.2003.08.011.

Fagents, S.A., 2003. Considerations for effusive cryovolcanism on Europa: The post-Galileo perspective. Journal of Geophysical Research: Planets 108, 5139. https://doi.org/10.1029/2003JE002128.

Fifer, L.M., Catling, D.C. and Toner, J.D., 2022. Chemical fractionation modeling of plumes indicates a gas-rich, moderately alkaline Enceladus ocean. The Planetary Science Journal 3, 191. https://doi.org/10.3847/PSJ/ac7a9f.

Fox-Powell, M.G. and Cousins, C.R., 2021. Partitioning of crystalline and amorphous phases during freezing of simulated Enceladus ocean fluids. Journal of Geophysical Research: Planets, 126, e2020JE006628. https://doi.org/10.1029/2020JE006628.

Fu, X., Jamison, M., Jubb, A.M., Liao, Y., Aspin, A., Hayes, K., Glein, C.R. and Yang, Z., 2020 a. Effect of copper salts on hydrothermal oxidative decarboxylation: a study of phenylacetic acid. Chemical Communications 56, 2791-2794. https://doi.org/10.1039/C9CC09825A.

Fu, X., Liao, Y., Glein, C.R., Jamison, M., Hayes, K., Zaporski, J. and Yang, Z., 2020b. Direct synthesis of amides from amines and carboxylic acids under hydrothermal conditions. ACS Earth and Space Chemistry 4, 722-729. https://doi.org/10.1021/acsearthspacechem.0c00009.

Glavin, D.P., Callahan, M.P., Dworkin, J.P. and Elsila, J.E., 2010. The effects of parent body processes on amino acids in carbonaceous chondrites. Meteoritics & Planetary Science 45, 1948-1972. https://doi.org/10.1111/j.1945-5100.2010.01132.x.

Glavin, D.P., McLain, H.L., Dworkin, J.P., Parker, E.T., Elsila, J.E., Aponte, J.C., Simkus, D.N., Pozarycki, C.I., Graham, H.V., Nittler, L.R. and Alexander, C.M.O.D., 2020. Abundant extraterrestrial amino acids in the primitive CM carbonaceous chondrite Asuka 12236. Meteoritics & Planetary Science 55, 1979-2006. https://doi.org/10.1111/maps.13560.

Glein, C.R. and Waite, J.H., 2020. The carbonate geochemistry of Enceladus' ocean. Geophysical Research Letters 47, e2019GL085885. https://doi.org/10.1029/2019GL085885.

Goguen, J.D., Buratti, B.J., Brown, R.H., Clark, R.N., Nicholson, P.D., Hedman, M.M., Howell, R.R., Sotin, C., Cruikshank, D.P., Baines, K.H. and Lawrence, K.J., 2013. The temperature and width of an active fissure on Enceladus measured with Cassini VIMS during the 14 April 2012 South Pole flyover. Icarus 226, 1128-1137. https://doi.org/10.1016/j.icarus.2013.07.012.

Guzman, M., Lorenz, R., Hurley, D., Farrell, W., Spencer, J., Hansen, C., Hurford, T., Ibea, J., Carlson, P. and McKay, C.P., 2019. Collecting amino acids in the Enceladus plume. International Journal of Astrobiology 18, 47-59. https://doi.org/10.1017/S1473550417000544.

Hamerly, T., Tripet, B., Wurch, L., Hettich, R.L., Podar, M., Bothner, B. and Copié, V., 2015. Characterization of Fatty Acids in Crenarchaeota by GC-MS and NMR. Archaea 2015, 472726. https://doi.org/10.1155/2015/472726.

Hand, K.P., Chyba, C.F., Priscu, J.C., Carlson, R.W. and Nealson, K.H., 2009 Astrobiology and the potential for life on Europa, in: Pappalardo, R.T., McKinnon, W.B., Khurana, K. (Eds.), Europa. University of Arizona Press, Tucson, pp. 589-629.

Hand, K.P., Murray, A., Garvin, J.B., and the Europa Lander Mission Concept Team, 2016. Europa Lander Study 2016 Report. https://europa.nasa.gov/resources/58/europa-lander-study-2016-report (accessed 26 October 2023).

Hand, K.P., Phillips, C.B., Murray, A., Garvin, J.B., Maize, E.H., Gibbs, R.G., Reeves, G., San Martin, A.M., Tan-Wang, G.H., Krajewski, J., Hurst, K., et al., 2022. Science goals and mission architecture of the Europa lander mission concept. The Planetary Science Journal, 3, 22. https://doi.org/10.3847/PSJ/ac4493.

Hemingway, D.J. and Mittal, T., 2019. Enceladus's ice shell structure as a window on internal heat production. Icarus 332, 111-131. https://doi.org/10.1016/j.icarus.2019.03.011.

Hendrix, A.R., Hurford, T.A., Barge, L.M., Bland, M.T., Bowman, J.S., Brinckerhoff, W., Buratti, B.J., Cable, M.L., Castillo-Rogez, J., Collins, G.C., Diniega, S., et al., 2019. The NASA roadmap to ocean worlds. Astrobiology 19, 1-27. https://doi.org/10.1089/ast.2018.1955.

Herboth, R., Gopakumar, G., Caleman, C. and Wohlert, M., 2021. Charge State Dependence of Amino Acid Propensity at Water Surface: Mechanisms Elucidated by Molecular Dynamics Simulations. J. Phys. Chem. A 125, 4705–4714. https://doi.org/10.1021/acs.jpca.0c10963.

Hsu, H.W., Postberg, F., Sekine, Y., Shibuya, T., Kempf, S., Horányi, M., Juhász, A., Altobelli, N., Suzuki, K., Masaki, Y., Kuwatani, T., et al., 2015. Ongoing hydrothermal activities within Enceladus. Nature 519, 207-210. https://doi.org/10.1038/nature14262.

Ingersoll, A.P. and Nakajima, M., 2016. Controlled boiling on Enceladus. 2. Model of the liquid-filled cracks. Icarus 272, 319-326. https://doi.org/10.1016/j.icarus.2015.12.040.

Kaplan, H.H., Milliken, R.E. and Alexander, C.M.O.'D., 2018. New constraints on the abundance and composition of organic matter on Ceres. Geophysical Research Letters 45, 5274-5282. https://doi.org/10.1029/2018GL077913.

Khawaja, N., Postberg, F., Hillier, J., Klenner, F., Kempf, S., Nölle, L., Reviol, R., Zou, Z. and Srama, R., 2019. Low-mass nitrogen-, oxygen-bearing, and aromatic compounds in Enceladean ice grains. Monthly Notices of the Royal Astronomical Society, 489, 5231-5243. https://doi.org/10.1093/mnras/stz2280.

Liao, Y., Aspin, A. and Yang, Z., 2022. Anaerobic oxidation of aldehydes to carboxylic acids under hydrothermal conditions. RSC Advances 12, 1738-1741.

Lobry, J.R. and Gautier, C., 1994. Hydrophobicity, expressivity and aromaticity are the major trends of amino-acid usage in 999 Escherichia coli chromosome-encoded genes. Nucleic acids research 22, 3174-3180. https://doi.org/10.1093/nar/22.15.3174.

MacKenzie, S.M., Neveu, M., Davila, A.F., Lunine, J.I., Cable, M.L., Phillips-Lander, C.M., Eigenbrode, J.L., Waite, J.H., Craft, K.L., Hofgartner, J.D., McKay, C.P., et al., 2022. Science objectives for flagship-class mission concepts for the search for evidence of life at Enceladus. Astrobiology 22, 685-712. https://doi.org/10.1089/ast.2020.2425.

Madigan, M., Martinko, J., Stahl, D. and Clark, D., 2012. Brock Biology of Microorganisms (13th Ed.) Pearson Education, San Francisco, p. 51.

Marsh, A., Miles, R. E. H., Rovelli, G., Cowling, A. G., Nandy, L., Dutcher, C. S. and Reid, J. P., 2017. Influence of Organic Compound Functionality on Aerosol Hygroscopicity: Dicarboxylic Acids, Alkyl-Substituents, Sugars and Amino Acids. Atmospheric Chem. Phys 17, 5583–5599. https://doi.org/10.5194/acp-17-5583-2017.

Martins, Z., Alexander, C.M.O.'D., Orzechowska, G.E., Fogel, M.L. and Ehrenfreund, P., 2007. Indigenous amino acids in primitive CR meteorites. Meteoritics & Planetary Science 42, 2125-2136. https://doi.org/10.1111/j.1945-5100.2007.tb01013.x.

McCollom, T.M., Ritter, G. and Simoneit, B.R., 1999. Lipid synthesis under hydrothermal conditions by Fischer-Tropsch-type reactions. Origins of Life and Evolution of the Biosphere 29, 153-166. https://doi.org/10.1023/A:1006592502746.

McCollom, T.M. and Seewald, J.S., 2006. Carbon isotope composition of organic compounds produced by abiotic synthesis under hydrothermal conditions. Earth and Planetary Science Letters 243, 74-84. https://doi.org/10.1016/j.epsl.2006.01.027.

Melwani Daswani, M., Vance, S.D., Mayne, M.J. and Glein, C.R., 2021. A metamorphic origin for Europa's ocean. Geophysical Research Letters 48, e2021GL094143. https://doi.org/10.1029/2021GL094143.

Miller, M.E., Burke, S.E. and Continetti, R.E., 2022. Production and impact characterization of Enceladus ice grain analogues. ACS Earth and Space Chemistry 6, 1813-1822. https://doi.org/10.1021/acsearthspacechem.2c00087.

Nakajima, M. and Ingersoll, A.P., 2016. Controlled boiling on Enceladus. 1. Model of the vapor-driven jets. Icarus 272, 309-318. https://doi.org/10.1016/j.icarus.2016.02.027.

Naraoka, H., Takano, Y., Dworkin, J.P., Oba, Y., Hamase, K., Furusho, A., Ogawa, N.O., Hashiguchi, M., Fukushima, K., Aoki, D., Schmitt-Kopplin, P., et al., 2023. Soluble organic molecules in samples of the carbonaceous asteroid (162173) Ryugu. Science 379, eabn9033. https://doi.org/10.1126/science.abn9033.

Neveu, M., Desch, S.J., Shock, E.L. and Glein, C.R., 2015. Prerequisites for explosive cryovolcanism on dwarf planet-class Kuiper belt objects. Icarus 246, 48-64. https://doi.org/10.1016/j.icarus.2014.03.043.

Nishikawa, K. and Ooi, T., 1982. Correlation of the amino acid composition of a protein to its structural and biological characters. The Journal of Biochemistry 91, 1821-1824. https://doi.org/10.1093/oxfordjournals.jbchem.a133877.

NIST, 2023. Chemistry WebBook, SRD 69. https://webbook.nist.gov/cgi/cbook.cgi?ID=64-19-7 (accessed 24 October 2023).

Parker, E.T., McLain, H.L., Glavin, D.P., Dworkin, J.P., Elsila, J.E., Aponte, J.C., Naraoka, H., Takano, Y., Tachibana, S., Yabuta, H., Yurimoto, H., et al., 2023. Extraterrestrial amino acids and amines identified in asteroid Ryugu samples returned by the Hayabusa2 mission. Geochimica et Cosmochimica Acta 347, 42-57. https://doi.org/10.1016/j.gca.2023.02.017.

Peter, J.S., Nordheim, T.A. and Hand, K.P., 2023. Detection of HCN and diverse redox chemistry in the plume of Enceladus. Nature Astronomy. https://doi.org/10.1038/s41550-023-02160-0.

Porco, C.C., Helfenstein, P., Thomas, P.C., Ingersoll, A.P., Wisdom, J., West, R., Neukum, G., Denk, T., Wagner, R., Roatsch, T. and Kieffer, S., 2006. Cassini observes the active south pole of Enceladus. Science 311, 1393-1401. https://doi.org/10.1126/science.1123013.

Porco, C., DiNino, D. and Nimmo, F., 2014. How the geysers, tidal stresses, and thermal emission across the south polar terrain of Enceladus are related. The Astronomical Journal 148, 45. https://doi.org/10.1088/0004-6256/148/3/45.

Postberg, F., Schmidt, J., Hillier, J., Kempf, S. and Srama, R., 2011. A salt-water reservoir as the source of a compositionally stratified plume on Enceladus. Nature 474, 620-622. https://doi.org/10.1038/nature10175.

Postberg, F., Khawaja, N., Abel, B., Choblet, G., Glein, C.R., Gudipati, M.S., Henderson, B.L., Hsu, H.W., Kempf, S., Klenner, F., Moragas-Klostermeyer, G., et al., 2018a. Macromolecular

organic compounds from the depths of Enceladus. Nature 558, 564-568. https://doi.org/10.1038/s41586-018-0246-4.

Postberg, F., Clark, R.N., Hansen, C.J., Coates, A.J., Dalle Ore, C.M., Scipioni, F., Hedman, M.M. and Waite, J.H., 2018b. Plume and surface composition of Enceladus, in: Schenk, P.M., Clark, R.N., Howett, C.J., Verbiscer, A.J. and Waite, J.H. (Eds.), Enceladus and the icy moons of Saturn. University of Arizona Press, Tucson, pp. 129-162. https://doi.org/10.2458/azu_uapress_97808165370075.

Postberg, F., Sekine, Y., Klenner, F., Glein, C.R., Zou, Z., Abel, B., Furuya, K., Hillier, J.K., Khawaja, N., Kempf, S., Noelle, L., et al., 2023. Detection of phosphates originating from Enceladus's ocean. Nature 618, 489-493. https://doi.org/10.1038/s41586-023-05987-9.

Pruppacher, H.R., Klett, J.D., Pruppacher, H.R. and Klett, J.D., 2010. Microphysics of clouds and precipitation, Springer, Dordrecht, pp. 191-215. https://doi.org/10.1007/978-0-306-48100-0_7.

Quick, L.C., Glaze, L.S. and Baloga, S.M., 2017. Cryovolcanic emplacement of domes on Europa. Icarus 284, 477-488. https://doi.org/10.1016/j.icarus.2016.06.029.

Roth, L., Saur, J., Retherford, K.D., Strobel, D.F., Feldman, P.D., McGrath, M.A. and Nimmo, F., 2014. Transient water vapor at Europa's south pole. Science 343, 171-174. https://doi.org/10.1126/science.1247051.

Ruesch, O., Platz, T., Schenk, P., McFadden, L.A., Castillo-Rogez, J.C., Quick, L.C., Byrne, S., Preusker, F., O'Brien, D.P., Schmedemann, N., Williams, D.A., et al. 2016. Cryovolcanism on Ceres. Science, 353, aaf4286. https://doi.org/10.1126/science.aaf4286.

Ruesch, O., Quick, L.C., Landis, M.E., Sori, M.M., Čadek, O., Brož, P., Otto, K.A., Bland, M.T., Byrne, S., Castillo-Rogez, J.C., Hiesinger, H., et al. 2019. Bright carbonate surfaces on Ceres as remnants of salt-rich water fountains. Icarus, 320, 39-48. https://doi.org/10.1016/j.icarus.2018.01.022.

Schmidt, J., Brilliantov, N., Spahn, F. and Kempf, S., 2008. Slow dust in Enceladus' plume from condensation and wall collisions in tiger stripe fractures. Nature 451, 685-688. https://doi.org/10.1038/nature06491.

Scully, J.E.C., Schenk, P.M., Castillo-Rogez, J.C., Buczkowski, D.L., Williams, D.A., Pasckert, J.H., Duarte, K.D., Romero, V.N., Quick, L.C., Sori, M.M. and Landis, M.E., 2020. The varied sources of faculae-forming brines in Ceres' Occator crater emplaced via hydrothermal brine effusion. Nature Communications, 11, 3680. https://doi.org/10.1038/s41467-020-15973-8.

Shock, E.L., 1993. Hydrothermal dehydration of aqueous organic compounds. Geochimica et Cosmochimica Acta 57, 3341-3349. https://doi.org/10.1016/0016-7037(93)90542-5.

Spencer, J.R., Nimmo, F., Ingersoll, A.P., Hurford, T.A., Kite, E.S., Rhoden, A.R., Schmidt, J. and Howett, C.J.A., 2018. Plume origins and plumbing: from ocean to surface, in: Schenk, P.M., Clark, R.N., Howett, C.J., Verbiscer, A.J. and Waite, J.H. (Eds.), Enceladus and the icy moons of Saturn. University of Arizona Press, Tucson, pp. 163-174. https://doi.org/10.2458/azu_uapress_97808165370075.

Steddum, R.E., 1971. Characteristics of Water Sprays under Vacuum Conditions. PhD dissertation, Louisiana State University. https://www.proquest.com/openview/a8b7bf09d8000b0a9c15667235e422d2/1.

Steel, E.L., Davila, A. and McKay, C.P., 2017. Abiotic and biotic formation of amino acids in the Enceladus ocean. Astrobiology 17, 862-875. https://doi.org/10.1089/ast.2017.1673

Thomas, P.C., Tajeddine, R., Tiscareno, M.S., Burns, J.A., Joseph, J., Loredo, T.J., Helfenstein, P. and Porco, C., 2016. Enceladus's measured physical libration requires a global subsurface ocean. Icarus 264, 37-47. https://doi.org/10.1016/j.icarus.2015.08.037.

Thomas, E.C., Vu, T.H., Hodyss, R., Johnson, P.V. and Choukroun, M., 2019. Kinetic effect on the freezing of ammonium-sodium-carbonate-chloride brines and implications for the origin of Ceres' bright spots. Icarus 320, 150-158. https://doi.org/10.1016/j.icarus.2017.12.038.

Trumbo, S.K., Becker, T.M., Brown, M.E., Denman, W.T., Molyneux, P., Hendrix, A., Retherford, K.D., Roth, L. and Alday, J., 2022. A new UV spectral feature on Europa: Confirmation of NaCl in leading-hemisphere chaos terrain. The Planetary Science Journal 3, 27. https://doi.org/10.3847/PSJ/ac4580.

Tosi, F., Mura, A., Cofano, A. et al., 2023. Salts and organics on Ganymede's surface observed by the JIRAM spectrometer onboard Juno. Nature Astronomy, https://doi.org/10.1038/s41550-023-02107-5.

Vance, S.D., Craft, K.L., Shock, E., Schmidt, B.E., Lunine, J., Hand, K.P., McKinnon, W.B., Spiers, E.M., Chivers, C., Lawrence, J.D., Wolfenbarger, N., et al., 2023. Investigating Europa's Habitability with the Europa Clipper. Space Science Reviews 219, 81. https://doi.org/10.1007/s11214-023-01025-2.

Villanueva, G.L., Hammel, H.B., Milam, S.N., Kofman, V., Faggi, S., Glein, C.R., Cartwright, R., Roth, L., Hand, K.P., Paganini, L., Spencer, J., et al., 2023a. JWST molecular mapping and characterization of Enceladus' water plume feeding its torus. Nature Astronomy 7, 1056-1062. https://doi.org/10.1038/s41550-023-02009-6.

Villanueva, G.L., Hammel, H.B., Milam, S.N., Faggi, S., Kofman, V., Roth, L., Hand, K.P., Paganini, L., Stansberry, J., Spencer, J., Protopapa, S., et al., 2023b. Endogenous CO_2 ice mixture on the surface of Europa and no detection of plume activity. Science 381, 1305-1308. https://doi.org/10.1126/science.adg4270.

Vu, T.H., Choukroun, M., Hodyss, R. and Johnson, P.V., 2020. Probing Europa's subsurface ocean composition from surface salt minerals using in-situ techniques. Icarus 349, 113746. https://doi.org/10.1016/j.icarus.2020.113746.

Vu, T.H., Hodyss, R., Johnson, P.V. and Cable, M.L., 2023. Spatial Distribution of Glycine and Aspartic Acid in Rapidly Frozen Brines Relevant to Enceladus. The Planetary Science Journal 4, 156. https://doi.org/10.3847/PSJ/aced90.

Waite, J.H., Glein, C.R., Perryman, R.S., Teolis, B.D., Magee, B.A., Miller, G., Grimes, J., Perry, M.E., Miller, K.E., Bouquet, A., Lunine, J.I., et al., 2017. Cassini finds molecular hydrogen in the Enceladus plume: evidence for hydrothermal processes. Science 356, 155-159. https://doi.org/10.1126/science.aai8703.

Supplementary Material to "Effect of the liquid-vacuum transition on the relative abundances of amino and fatty acids sought as biosignatures on icy ocean worlds"

Marc Neveu[1,2,*], Alexandria Aspin[3,*], Mariam Naseem[1], and Ziming Yang[3]

[1] University of Maryland, College Park, MD, USA
[2] NASA Goddard Space Flight Center, Greenbelt, MD, USA
[3] Department of Chemistry, Oakland University, Rochester, MI, USA
[*] These authors contributed equally to this manuscript.

S1. Velocity and freezing rate of the fluid and grains

The speed of the fluid and grains in the sub-P_t sections of the injection line, v_{fluid}, was likely on the order of 10 m s^{-1}. Below, we provide estimates and constraints on this velocity using different methods. First, the flow velocity was greater than $\sim (g \times l)^{0.5} \approx 1$ m s^{-1} because the material sprayed the center of the collection cup at a distance $l \approx$ 5–15 cm from the end of the port at the chamber edge, rather than falling to the bottom of the chamber due to Earth's gravitational acceleration g.

Second, we think that the grain velocity was not much greater than 1 m s^{-1}, because grains did not bounce off of the cup or visibly pit its soft aluminum surface. In vacuum, 10–100 μm particles bounce only for impact speeds > 0.1–1 m s^{-1} (Musiolik et al., 2016; Nietiadi et al, 2020; Arakawa & Krijt, 2021; Fritscher & Teiser, 2021). Higher velocities are possible for smaller (Miller et al., 2022) and/or partially frozen, stickier particles, which may have been the case in our experiments.

Third, we did not observe water (liquid or ice) in grains during injection, except a few instances of > mm-sized, partially frozen material that volatilized within ~1 second. Frozen grains may have been too small to be visible (< 0.1 mm), the freezing time scale discussed in Section 2.1 of the main text indicates a corresponding transport time of ≤ 0.005 s. Since transport takes place through the ≈ 20–30 cm distance between the valves and collection cup (see Fig. 2a of the main text), a corresponding lower bound on v_{fluid} is 40 m s^{-1}.

Finally, we witnessed impacting sub-mm grains on the cup temporarily tilting its foil support by $d_{tilt} \sim 1$ cm (Supplementary video), and reproduced this tilt by placing a test mass m_{test} = 8 grams on a horizontal foil sheet. By equating $m_{test}\, g \approx m_{grain}\, v_{fluid}^2/d_{tilt}$, with v_{fluid}^2/d_{tilt} the approximate grain deceleration to zero velocity, we find $v_{fluid} \approx (d_{tilt}\, m_{test}\, g / m_{grain})^{0.5} = 14$ m s^{-1} for

a 1 mm-radius ice grain. These ~10 m s^{-1} velocities are similar to those modeled for most of the length of subsurface conduits with pressure below P_t on Enceladus (Nakajima & Ingersoll, 2016).

Compound	Mass of recovered dry residue (% of total injected mass, ± 1 standard deviation)			
	Valves	Flange	Port	Chamber
Gly	12.3±8.1	24.2±4.8	63.2±10.9	9.1±1.1
Ala	12.2±8.2	26.5±6.5	63.6±16.8	8.4±3.6
Glu	9.8±6.1	22.1±5.5	49.2±10.3	8.6±1.4
Asp	7.7±4.5	16.0±3.8	36.2±8.3	6.1±1.3
Leu	13.1±7.9	22.1±5.4	50.9±12.4	7.3±3.9
Thr	13.4±9.2	29.7±6.5	71.3±17.6	7.3±0.5
AIB	8.7±5.8	15.7±3.1	36.2±6.3	6.2±1.1
γAB	10.0±6.7	20.8±4.2	47.3±10.5	7.8±1.8
His	8.1±2.5	21.5±6.4	47.8±8.6	10.1±1.4
Phe	19.4±1.2	23.7±6.9	52.1±8.0	12.4±2.5
Tyr	11.0±4.3	15.6±5.1	29.8±8.0	6.0±1.7
Trp	7.4±5.6	16.2±5.2	32.6±7.4	4.0±0.9
Phenylacetic acid	0.86 [a]	10.2±0.4	62.1±3.2	6.6±1.1
Palmitic acid	0.95 [a]	2.86±0.04	5.20±0.01	0.92±0.01

Table S1. *Fraction of the mass of compound recovered in various sections of the injection path. Uncertainties are 1 standard deviation across three 200 mL solution replicates (amino acid injection) or the standard deviation, unweighted by volume, across two 280-mL and 470-mL replicates of the fatty acid solution.* [a] *Only one replicate; for the other, the phenylacetic acid signal was below the GC limit of detection.*

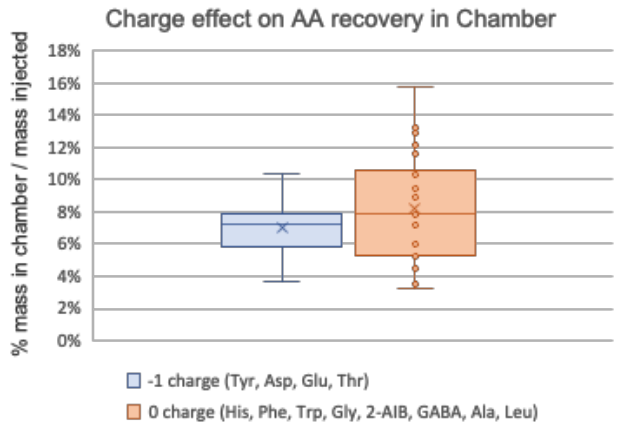

Figure S1. *Effect of overall charge of amino acids on the mass fraction of amino acid recovered in the chamber (% of injected mass). The predominant form of Tyr, Asp, Glu, and Thr had an overall charge of -1, while the others were electrically neutral.*

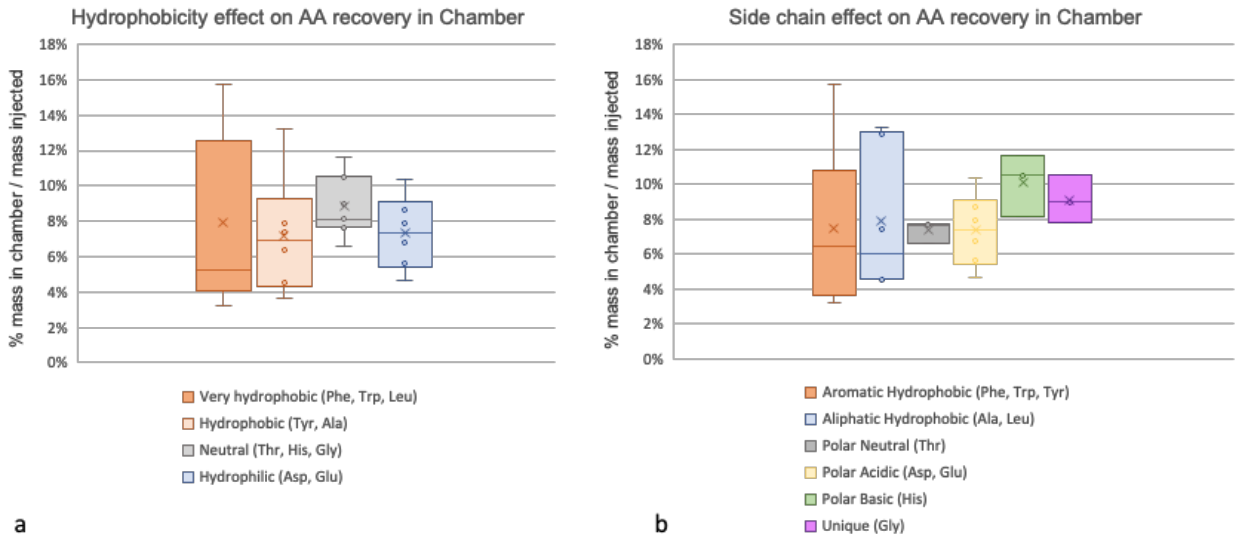

Figure S2. *Effect of hydrophobicity* ***(a)*** *and side chain functionality* ***(b)*** *of amino acids on the mass fraction in the collection chamber (as % of injected mass) after simulated plume injection. Four of the amino acids are aromatic, including Phe, Tyr, Trp, and His, which contain either six- or five-membered rings. Phe and Tyr are quite similar in their structures, with a short carbon chain attached to a benzene ring (Phe) or to the para-position of a benzenol (Tyr). Trp is the largest aromatic acid, which contains an indole group as the side chain. Because these aromatic side chains are relatively bulky and nonpolar, Phe, Tyr, and Trp are classified under the aromatic-hydrophobic category for comparison with other amino acids (Fig. S2). His, on the other hand, although aromatic with an imidazole group in the side chain, is considered a polar-basic amino acid because the imidazole group is readily protonated in solutions. For non-aromatic structures, Ala and Leu are categorized as aliphatic-hydrophobic because their side chains contain only aliphatic hydrocarbons and are hydrophobic in nature. Asp and Glu both have a carboxyl group in their side chain, which is expected to deprotonate at the pH of injected solutions, making them polar-acidic. The side chain of Thr consists of a short hydrocarbon with an alcohol group attached, which is relatively polar but neutral at the experimental conditions; so Thr is considered polar-neutral. As a reference, Gly is given its own unique category due to its simplest structure.*

Supplementary video (Neveu_Supp_VID_20230209_155457.mp4)

Cup and foil stand, viewed from top, tilted by impacting grains.

References

Arakawa, S. and Krijt, S., 2021. On the stickiness of CO_2 and H_2O ice particles. The Astrophysical Journal 910, 130. https://doi.org/10.3847/1538-4357/abe61d.

Fritscher, M. and Teiser, J., 2021. CO_2-ice Collisions: A New Experimental Approach. The Astrophysical Journal 923, 134. https://doi.org/10.3847/1538-4357/ac2df4.

Miller, M.E., Burke, S.E. and Continetti, R.E., 2022. Production and impact characterization of Enceladus ice grain analogues. ACS Earth and Space Chemistry 6, 1813-1822. https://doi.org/10.1021/acsearthspacechem.2c00087.

Musiolik, G., Teiser, J., Jankowski, T. and Wurm, G., 2016. Ice grain collisions in comparison: CO_2, H_2O, and their mixtures. The Astrophysical Journal 827, 63. https://doi.org/10.3847/0004-637X/827/1/63.

Nietiadi, M.L., Rosandi, Y. and Urbassek, H.M., 2020. Collisions between ice-covered silica grains: An atomistic study. Icarus 352, 113996. https://doi.org/10.1016/j.icarus.2020.113996.